Materials Today • Volume xxx, Number xx • xxxx 2021 RESEARCH

ELSEVIER

Structural insights into composition design of Li-rich layered cathode materials for high-energy rechargeable battery

Chong Yin [a,f,#], Zhining Wei [a,j,#], Minghao Zhang [b,#], Bao Qiu [a,f,*], Yuhuan Zhou [a,f], Yinguo Xiao [c], Dong Zhou [a], Liang Yun [a], Cheng Li [d], Qingwen Gu [a], Wen Wen [e], Xiao Li [a,f], Xiaohui Wen [a,f], Zhepu Shi [a,k], Lunhua He [g,h,i], Ying Shirley Meng [b,*], Zhaoping Liu [a,f,*]

[a] Ningbo Institute of Materials Technology & Engineering (NIMTE), Chinese Academy of Sciences, Ningbo 315201, PR China
[b] Department of NanoEngineering, University of California San Diego (UCSD), La Jolla, CA 92093, USA
[c] School of Advanced Materials, Peking University, Shenzhen Graduate School, Shenzhen 518055, PR China
[d] Neutron Scattering Division, Oak Ridge National Laboratory (ORNL), 1 Bethel Valley Road, Oak Ridge, TN 37831-6473, USA
[e] Shanghai Synchrotron Radiation Facility, Chinese Academy of Sciences, Zhangjiang High-Tech. Park, Pudong New Area, Shanghai 201204, PR China
[f] Center of Materials Science and Optoelectronics Engineering, University of Chinese Academy of Sciences (UCAS), Beijing 100049, PR China
[g] Beijing National Laboratory for Condensed Matter Physics, Institute of Physics, Chinese Academy of Sciences, Beijing 100190, PR China
[h] Spallation Neutron Source Science Center, Dongguan 523803, PR China
[i] Songshan Lake Materials Laboratory, Dongguan 523808, PR China
[j] School of Chemical Engineering and Technology, China University of Mining and Technology (CUMT), Xuzhou 221116, P. R. China
[k] University of Nottingham Ningbo China (UNNC), Taikang East Road 199, Ningbo 315100, P. R. China

The Li-rich layered oxide is considered as one of the most promising cathode materials for high energy density batteries, due to its ultrahigh capacity derived from oxygen redox. Although incorporating over-stoichiometric Li into layered structure can generate Li_2MnO_3-like domain and enhance the oxygen redox activity thermodynamically, the fast and complete activation of the Li_2MnO_3-like domain remains challenging. Herein, we performed a systematic study on structural characteristics of Li-rich cathode materials to decipher the factors accounting for activation of oxygen redox. We reveal that the activation of Li-rich cathode materials is susceptible to local Co coordination environments. The Co ions can intrude into Li_2MnO_3-like domain and modulate the electronic structure, thereby facilitating the activation of Li-rich layered cathode materials upon first charging, leading to higher reversible capacity. In contrast, Li_2MnO_3-like domain hardly contains any Ni ions which contribute little to the activation process. The optimum composition design of this class of materials is discussed and we demonstrate a small amount of Co/Mn exchange in Li_2MnO_3-like domain can significantly promote the oxygen redox activation. Our findings highlight the vital role of Co ions in the activation of oxygen redox Li-rich layered cathode materials and provide new insights into the pathway toward achieving high-capacity Li-rich layered cathode materials.

Keywords: Li-ion batteries; Li-rich layered cathodes; Oxygen redox activation; Composition design; Local structure modulation

* Corresponding authors.
E-mail addresses: Qiu, B. (qiubao@nimte.ac.cn), Shirley Meng, Y. (shirleymeng@ucsd.edu), Liu, Z. (liuzp@nimte.ac.cn).
# These authors contributed equally to the work.

 https://doi.org/10.1016/j.mattod.2021.10.020

Please cite this article in press as: C. Yin et al., Materials Today (2021), https://doi.org/10.1016/j.mattod.2021.10.020

Introduction

The application of lithium-ion batteries (LIBs) has expanded rapidly over the past decades [1–3]. Developing LIBs with higher energy density than current benchmarks remains attractive, especially for electric vehicle applications. The relatively low capacity of cathode materials is becoming the limiting factor for the future development of LIBs with high energy density [2]. Li-rich nickel–cobalt-manganese (LR-NCM) layered cathodes with over-stoichiometric Li have the potential to double the capacities of stoichiometric nickel–cobalt-manganese (NCM) layered cathode materials, due to a blend of cationic redox and anionic redox [4]. There is a growing consensus that such high capacities arise from the reversible redox of O^{2-} anions in Li_2MnO_3-like domain, which is identified as a nano-composite component in Li-rich cathode materials [5]. Incorporating more Li and Mn in Li-rich layered structure is thus regarded as a golden rule to achieve high capacity. The pursuit of high-Mn Li-rich layered cathodes is even more promising considering the resource availability of Mn compared with Ni. However, the practical capacity of Mn and Li-rich materials is highly dependent on the electrochemical activation process of Li_2MnO_3-like domain. Early studies have observed that a substantial amount of Li ions could be extracted from pure Li_2MnO_3, only when the activation potential is above 4.5 V vs. Li/Li^+ and the current density is small (10 mA g^{-1}) [6,7], which implies the poor kinetics of Li_2MnO_3. The challenge is thus how to consolidate more Li_2MnO_3-like domain in layered oxide while maintaining fast electrochemical activation process [8,9].

Composition design is a widely applied engineering strategy to improve the activation kinetics in Li-rich layered cathodes. The previous studies have identified that Co ions play a positive role in the activation of Li_2MnO_3-like domain, while Ni ions have little impact [10,11]. However, the interaction mechanism between Li_2MnO_3-like domain and Ni/Co ions is not investigated in the previous reports. Other cation doping, such as Na [12] and Fe [13] have been identified to improve reaction kinetics through reducing the barrier of Li ion diffusion. The doping of Cr was also proposed to improve the activation of Li_2MnO_3-like domain, given the strong covalence between transition metal and oxygen due to the close energy between the bottom of Cr-3d band and the top of O-2p band [14]. However, the missing structural analysis on the local coordination environments in these previous works makes the doping effect ambiguous. Recently, the microstructure and defect engineering have broken a new ground in activating the oxygen redox. The stacking faults of transition metal layers and oxygen vacancies have been introduced to facilitate the activation of Li_2MnO_3-like domain [15,16]. However, the complicated synthesis method for defect engineering limits its practical application. To formulate performance improvement guidelines for Li-rich layered oxides, the fundamental relationships should be studied among chemical compositions, microstructures and activation of Li_2MnO_3-like domain. As illustrated in Fig. 1, a comprehensive structure analysis requires samples with well controlled compositions, from stoichiometric NCM cathode to Li-rich Mn-based layered cathodes, and toolset for probing different length scales, from long-range to short-range ordering.

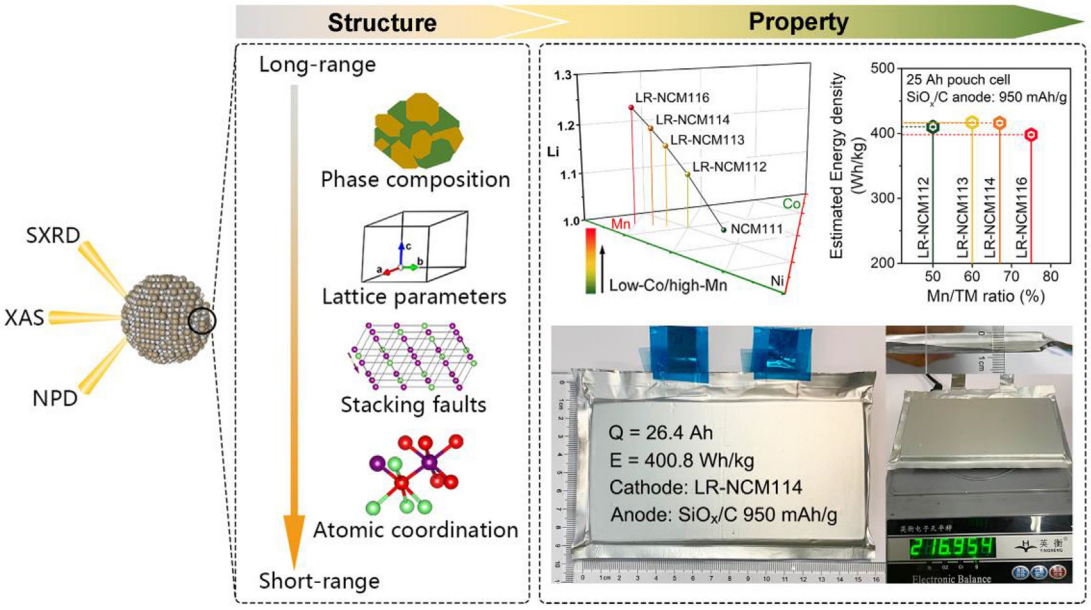

FIGURE 1

Schematic of pathway toward establishing relationships among chemical compositions, microstructures with electrochemical property in Li-rich Mn-based cathodes. Composition diagram shows a set of Ni-Co-Mn layered samples used in this work, with a nominal formula of $Li_{1+Y}[Ni_{2/(3+3X)}Co_{2/(3+3X)}Mn_{2X/(3+3X)}]O_2$ (LR-/NCM11X: $X = 1, 2, 3, 4, 6$; $Y \geq 0$). Fundamental understanding of structural information from long-range to short-range ordering is needed to improve electrochemical performance of low-Co/high-Mn cathode materials. The energy density of 25 Ah pouch cell is calculated using Li-rich cathode samples and SiO_x/C composite anode material with a specific capacity of 950 mAh g^{-1}. To verify the reliability of the estimation, a 400 Wh kg^{-1} pouch cell was fabricated and serves as an example of high energy rechargeable battery. More details are given in Supplementary Note 1.

Please cite this article in press as: C. Yin et al., Materials Today (2021), https://doi.org/10.1016/j.mattod.2021.10.020

In this study, we investigate the structural characteristics of LR-NCM and stoichiometric NCM layered materials, with a nominal formula of $Li_{1+Y}[Ni_{2/(3+3X)}Co_{2/(3+3X)}Mn_{2X/(3+3X)}]O_2$ (LR-/NCM11X: $X = 1, 2, 3, 4, 6$; $Y \geq 0$) as shown in Fig. 1. Synchrotron X-ray diffraction (SXRD) and time-of-flight neutron powder diffraction (TOF-NPD) were used to resolve the long-range structure for all the samples. The extended X-ray absorption fine structure (EXAFS) results exhibit the atomic coordination environments of each transition-metal. We reveal that Ni^{2+} coordination environments remain the same among all the samples, while Co^{3+} ions participate in the formation of Li_2MnO_3-like domain. Combined with electrochemical measurements, we demonstrate that the activation of Li_2MnO_3-like domain is highly related to the Co mixing in Li_2MnO_3-like domain. It is observed that the distortions of Co–O and Mn–O bonds greatly increase after cycling, which further manifests that the activated lattice oxygen ions are coordinated with Co and Mn. The sample with the optimized composition is able to deliver energy density of 400 Wh/kg at cell level on the basis of SiO_x/C anodes. These findings provide engineering guidelines for improving reaction kinetics of anionic redox and opportunities to achieve high energy density LIBs with Li-rich Mn-based layered oxides.

Material and methods

Materials synthesis

The detailed procedures of material preparation are similar to our previous report [17]. $LiNi_{1/3}Co_{1/3}Mn_{1/3}O_2$ (NCM111), $Li_{1.06}Ni_{0.22}Co_{0.22}Mn_{0.45}O_2$ (LR-NCM112), $Li_{1.11}Ni_{0.17}Co_{0.17}Mn_{0.50}O_2$ (LR-NCM113), $Li_{1.14}Ni_{0.13}Co_{0.13}Mn_{0.54}O_2$ (LR-NCM114) and $Li_{1.17}Ni_{0.095}Co_{0.095}Mn_{0.57}O_2$ (LR-NCM116) were synthesized by a solid-state method with carbonate precursors and Li_2CO_3 (*Sinopharm Chemical Reagent Co., Ltd., Shanghai, China*). The carbonate precursors were prepared by a co-precipitation method: stoichiometric amounts (Ni:Co:Mn = 1:1:1, 1:1:2, 1:1:3, 1:1:4 and 1:1:6) of $NiSO_4{\cdot}6H_2O$ (*Sinopharm Chemical Reagent Co., Ltd., Shanghai, China*), $CoSO_4{\cdot}7H_2O$ (*Sinopharm Chemical Reagent Co., Ltd., Shanghai, China*), and $MnSO_4{\cdot}5H_2O$ (*Sinopharm Chemical Reagent Co., Ltd., Shanghai, China* were dissolved in deionized water; then the aqueous solution with the reagent concentration of 2.0 mol L^{-1} was continuously pumped into a continuous stirring tank reactor (CSTR, 250 L); at the same time, Na_2CO_3 aqueous solution (2.0 mol L^{-1}) and NH_4OH aqueous solution (0.2 mol L^{-1}) were pumped into the CSTR, separately. During the reaction, the pH was kept at around 8.0 and the temperature was kept at 60 °C. The as-obtained co-precipitation powders were filtered, washed several times with deionized water, and then dried at 120 °C overnight. After mixing Li_2CO_3, the mixed precursors were pretreated at 500 °C for 5 h before calcining at 820 °C for 12 h in the air. The Li_2MnO_3 sample was synthesized by a solid-state method with stoichiometric amounts of Li_2CO_3 and $MnCO_3$ (*Sinopharm Chemical Reagent Co., Ltd., Shanghai, China*). After calcining at 820 °C for 12 h, the powders were ball milled under 800 rpm for 3 h.

Physical characterization

The in-house XRD pattern for Li_2MnO_3 sample was obtained by using a Bruker D8 X-ray diffractometer with a Cu Kα radiation source. SXRD patterns were collected at the beamline BL14B of the Shanghai Synchrotron Radiation Facility (SSRF) with the X-ray wavelength of 0.6887 Å. For the pristine materials, TOF-NPD patterns were collected at GPDD beamline of China Spallation Neutron Source (CSNS). For the cycled materials, the TOF-NPD patterns were collected on the POWGEN beamline at the Spallation Neutron Sources (SNS) in the Oak Ridge National Laboratory. The joint refinements were performed by using the GSAS-II program [18], based on the Rietveld method. The refined parameters include polynomial background parameters, overall atomic displacement parameter, lattice parameters, FWHM parameters (U, V and W), position of oxygen, occupancy of Li and Ni in rhombohedral R $\overline{3}$ m phase, occupancy of Li and Mn in monoclinic C2/m phase, and phase fraction. The FAULTS program [19] was used to analyze super-lattice peaks. For the pristine materials, the hard X-ray absorption spectroscopy (hXAS) experiments were carried out with transmission mode at beamline KMC-2 of the synchrotron BESSY at Helmholtz-Zentrum Berlin, Germany. For the cycled materials, the XAS experiments were carried out with transmission mode at beamline BL11B of the SSRF at Shanghai, China. The foils of Ni, Co and Mn were simultaneously measured for calibration. The X-ray absorption near edge structure (XANES) data and EXAFS data were processed and fitted using the ATHENA software package [20]. For normalization and background removal of XANES, the E_0 value was set by a default fraction of edge step (0.5). The pre-edge range was set between −150 eV and −30 eV relative to E_0, and the post-edge range was set from 150 eV to the maximum energy position of the XANES. The normalized k^3-weighted EXAFS spectra were Fourier-transformed (FT) in k space with integration limits of 3.0–10.5 $Å^{-1}$ for the Ni, Co and Mn. The least-square fits were carried out in R space between 1.0 Å and 3.0 Å. A field emission scanning electron microscope (FSEM, Hitachi S-4800) was used to analyze the morphology of pristine materials. The high-resolution transmission images were obtained from a double aberration-corrected JEOL-ARM 200CF microscope with a cold-field emission gun operated at 200 keV.

Electrochemical measurements

Electrochemical performances of LR-/NCM11X ($X = 1, 2, 3, 4, 6, 8$) samples were tested in CR2032-type coin cells using a LAND-CT2001A battery test system. Electrodes consisted of 80 wt.% LR-/NCM11X ($X = 1, 2, 3, 4, 6, 8$) samples, 10 wt.% super P carbon, and 10 wt.% polyvinylidene fluoride (PVDF) binder. Coin cells were assembled with circular cathode electrodes, Celgard 2502 separator, and thin Li metal foil in an argon-filled glove box. The moisture and oxygen levels of the argon-filled glove box were less than 0.1 ppm. The electrolyte was mixed with ethylene and dimethyl carbonate (3:7 volume ratio) with $LiPF_6$ (1.0 M). The cells were tested by galvanostatic charge–discharge mode in the potential range of 2.0–4.8 V *vs.* Li^+/Li^0. The nominal capacity of the samples was set to 250 mAh g^{-1}. The mass loading of cathode materials was about 5 mg cm^{-2}. The positive electrodes for pouch cells were prepared by mixing 95 wt.% of samples, 2 wt.% of super P carbon, and 3 wt.% of PVDF. The anode materials were lithium metal foils (pouch cells used to collect cycled samples for TOF-NPD measurements) or SiO_x/C composite (pouch cell used to verify high energy density). For coin cells, the amount of electrolyte was 20 μL. For pouch cells, the

Please cite this article in press as: C. Yin et al., Materials Today (2021), https://doi.org/10.1016/j.mattod.2021.10.020

weight of electrolyte was about 2.0 g Ah^{-1}. The powder conductivity was tested by using an ST2742B electro-conductibility tester (Suzhou Jingge Electronic Co., Ltd.) based on four-probe method. The galvanostatic intermittent titration technique (GITT) was tested with 30 min pulse and 2 h rest. The pulse current density was 0.05 C. The electrochemical impedance spectroscopy (EIS) was tested on Solartron Analytical system with an amplitude of 10 mV over a frequency range of 100 kHz–0.0 1 Hz. All batteries in this study were tested at room temperature. A simplified method with the following formula was applied to calculate Li diffusion coefficient [21]:

$$D_{Li^+} = \frac{4}{\pi\tau}\left(\frac{mV_M}{MS}\right)^2\left(\frac{\Delta E_s}{\Delta E_\tau}\right)^2$$

Results

Long-range structure characterization

In order to obtain the crystal structure information of the synthesized LR-/NCM materials, the SXRD/NPD joint *Rietveld* refinements were carried out and the patterns are plotted in Fig. 2a–e. The detailed results of refined parameters are summarized in Tables S1 and S2. The patterns of NCM111 sample can be indexed with a single rhombohedral R $\overline{3}$ m phase without impurities [26]. Monoclinic Li_2MnO_3-like domain (Space group: C2/m) with $LiMn_6$ ordering appears in LR-NCM11X (X = 2, 3, 4, 6) samples, corresponding to the super-lattice diffraction peaks located in the 2θ region between 7.5° and 15° [22]. The Joint *Rietveld* refinement for NCM111 sample was carried out using a single rhombohedral R $\overline{3}$ m phase (R phase) and the refinements for LR-NCM11X (X = 2, 3, 4, 6) samples were performed using the two-phase model with the addition of monoclinic C2/m phase (M phase). The weighted profile factors (R_{wp}) for all the samples are less than 10%, indicating that the applied model fits well for the samples.

For comparison, the lattice parameters a, b and c of M phase were converted into a', b' and c', which have the similar R-phase-like characteristics (Supplementary Note 2 and Fig. S1). As shown in Fig. 2f, the lattice parameter a reduces from 2.861 Å to 2.848 Å with X increasing in LR-/NCM11X (from X = 1 to X = 6), and a' (b') reduced from 2.860 Å (2.853 Å) to 2.850 Å (2.848 Å). The lattice parameters c (R phase) remains nearly constant (see Fig. 2g), while the parameters c' (M phase) declines from 14.257 Å to 14.234 Å. The lattice parameters shrink with increasing Mn content because of shorter bond distance of Mn-O (as proven by EXAFS fittings in latter section). The quantitative phase analysis shows that the amount of Li_2MnO_3-like domain increases from 25.3% to 61.3% with X increasing values in LR-NCM11X (from X = 2 to X = 6). These values are consistent with the calculated numbers based on the nominal two-phase formula of $xLi_2MnO_3{\cdot}(1-x)LiMO_2$ (M = Ni, Co, Mn) [8]. The subtle difference between the refined and calculated values for the Li-rich layered cathode may result from the microstrain due to multi-domain composition, as shown in Fig. S2. The refined interlayer Li_{3a}/Ni_{3b} mixing degree in R phase is lower than 3% (Fig. 2i), which indicates that the anti-site defects are not prevailing in LR-/NCM11X (X = 1, 2, 3, 4, 6) samples. The refined intralayer Li_{2b}/Mn_{4g} mixing degree in M phase is much higher, ranging from 50.5% to 39.1% in LR-NCM11X (X = 2, 3, 4, 6) samples. The high interlayer Li_{2b}/Mn_{4g} mixing degree of high Ni/Co samples (e.g. LR-NCM112) indicates that the increase of Ni/Co content can inhibit the formation and segregation of Li_2MnO_3-like domain to some extent. Although the lower Li_{2b}/Mn_{4g} mixing degree often implies the more ordered $LiMn_6$ honeycomb structure in Li_2MnO_3-like domain, the local Li-Mn coordination environments cannot be obtained from the refinements because *Rietveld* method is based on average crystal structure [23].

Short-range structure characterization

The schematic illustration of the composite structure is shown in Fig. 3a, and two types of local structural configurations are highlighted as follows. The black solid box exemplifies the out-of-plane stacking ordering in the monoclinic domain. Three different stacking orientations of transition metal layers (Fig. 3b) can potentially create the so-called stacking faults [24]. The other type of local structural configuration is in-plane cationic ordering (Fig. 3c), such as the $LiMn_6$ honeycomb structure in Li_2MnO_3-like domain. Fig. 3d shows the super-lattice peaks of LR-NCM11X (X = 2, 3, 4, 6) samples, and the broadening of super-lattice peaks implies the stacking faults of transition metal layers [19]. NCM111 is not discussed here because there is no $LiMn_6$ honeycomb structure in transition metal layers for NCM111 [25]. A two-layer model [17] was applied to simulate the super-lattice peaks by using FAULTS program [19]. Note that the probability of stacking faults used in the following section is calculated by the formula proposed in the previous study [24]. Fig. S3a shows the simulated super-lattice peaks with various probabilities of stacking faults, displaying the drastic intensity decreasing with the increasing of stacking faults. However, the obvious peak broadening between 9.0° and 9.2°, as marked by arrow in Fig. 3d, cannot be solely ascribed to stacking faults.

Besides the stacking faults, the size effect of M phase can also induce super-lattice peaks broadening (Fig. 3c). According to this hypothesis, we further introduced the parameters D_g and D_l in our simulation as an indicator of the Li_2MnO_3-like domain length (calculation details are given in Supplementary Note 3). Fig. S3b shows the simulated super-lattice peaks with different domain lengths (D_g and D_l were set to equal for simplicity). The broadening of the super-lattice peaks between 9.0° and 9.2° is consistent with our experimental results in Fig. 3d. Therefore, the super-lattice peaks of LR-NCM11X (X = 2, 3, 4, 6) samples were refined in consideration of both stacking faults and domain length effect (Fig. S4). The refined probability of stacking faults and domain lengths are plotted in Fig. 3e. All samples show high probability of stacking faults (>45%), implying that the chemical compositions have no obvious impact on stacking ordering. The high degrees of stacking faults are probably due to the nature of carbonate precursors and calcination process we applied [26]. The domain lengths of LR-NCM112 and LR-NCM114 are less than 200 Å, while LR-NCM113 and LR-NCM116 samples exhibit large domain lengths beyond 700 Å. This indicates that ordering of $LiMn_6$ honeycomb structure in Li_2MnO_3-like domain is sensitive to composition and there exists a nonlinear relation.

To decipher the atomic-scale local structure, XANES and EXAFS measurements were carried out on Ni, Co and Mn K-

Please cite this article in press as: C. Yin et al., Materials Today (2021), https://doi.org/10.1016/j.mattod.2021.10.020

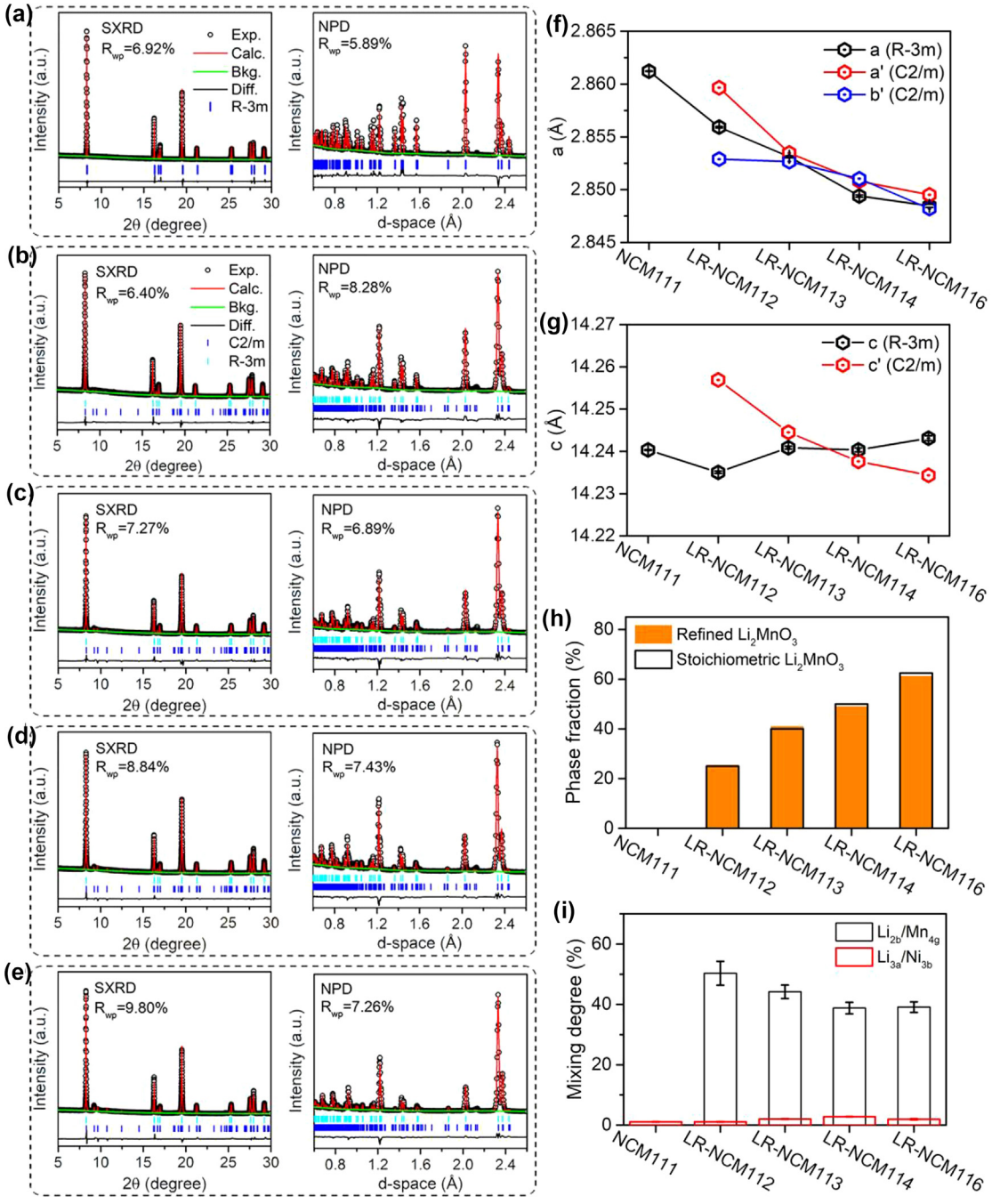

FIGURE 2

Long-range structural analysis for different samples. (a–e) The Joint *Reitveld* refinement patterns of synchrotron X-ray diffraction and neutron diffraction for NCM111, LR-NCM112, LR-NCM113, LR-NCM114 and LR-NCM116, respectively. (f,g) Comparison of lattice parameters for different samples (the details for calculating a', b' and c' were given in Supplementary Note 2). (h) Comparison of refined phase fraction and stoichiometric phase fraction of Li_2MnO_3 based on the nominal two-phase formula. (i) Comparison of Li_{3a}/Ni_{3b} mixing degree (R phase) and Li_{2b}/Mn_{4g} mixing degree (M phase) for different samples.

edges. The similar XANES spectra of Ni, Co and Mn for different X values of NCM11X demonstrate that the oxidation states of Ni, Co and Mn in NCM11X samples with different X values (X = 2, 3, 4, 6) are almost the same (Fig. 4a). According to the previous research on NCM111 [27], the oxidation states of Ni, Co and Mn should be +2, +3 and +4, respectively. A theoretical atomic coordination model can be established based on Pauling's electrostatic valence rule [28]. As shown in Fig. 4b, the layered structure contains multiple atomic coordination configurations. Here, a semiquantitative equation is applied to evaluate the stability of a coordination configuration:

$$\Delta Z = \left| Z_A - \Sigma \frac{Zc}{n} \right|$$

where Z_A is the valence of anion and Zc is the valence of cations. Number n is coordination number of the central anion. The summation notation represents summing over all coordinate cations.

Please cite this article in press as: C. Yin et al., Materials Today (2021), https://doi.org/10.1016/j.mattod.2021.10.020

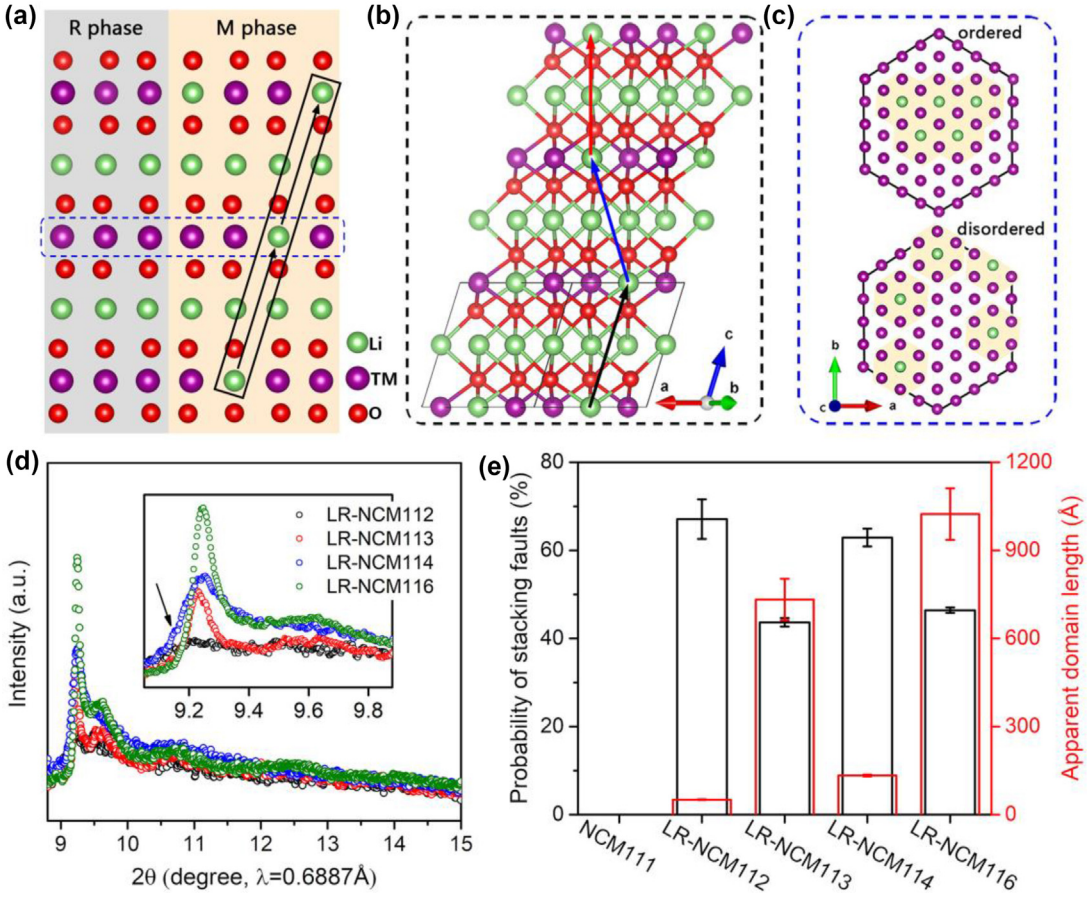

FIGURE 3

Short-range structural analysis for out-of-plane stacking ordering and in-plane ordering. (a) Structural illustration of typical Li-rich layered oxides cathode with a combination of rhombohedral domain (R domain) and monoclinic domain (M domain). The black solid box highlights the out-of-plane stacking ordering, and the blue dotted box indicates the in-plane ordering. (b) Schematic of stacking faults. Three possible transition vectors are colored with black, blue and red. (c) Schematic of in-plane cationic arrangement for the ordered and disordered $LiMn_6$ honeycomb structures. (d) Zoom-in SXRD patterns of super-lattice peaks for LR-/NCM11X (X = 1, 2, 3, 4, 6) samples. (e) Refinement results for LR-NCM11X (X = 2, 3, 4, 6) samples.

According to the principle of local electrical neutrality, the structure may become unstable if $\Delta Z > 0$. Three Li ions in the Li layer are always coordinated with central oxygen atom, while the coordination environments of cations in the transition metal layer may have different combinations. In the stable state ($\Delta Z = 0$), only three combinations (Co-Co-Co, Ni-Co-Mn, and Li-Mn-Mn) are feasible in the transition metal layer. We cannot exclude the existing of Li-Co-Mn, Ni-Ni-Mn and Mn-Mn-Ni combinations because its ΔZ ($\Delta Z = 1/6$) is close to 0. Considering the high ΔZ ($\Delta Z = 1/3$) value of Li-Mn-Ni or Li-Co-Co combination, it is almost impossible for these combinations to abound in LR-/NCM layered oxides.

Further justification of the atomic coordination is provided by the EXAFS analysis and the radial distribution function (RDF) patterns (Fig. 4c). Despite the different central cations, the first coordination shell refers to the nearest neighbor (NN) TM-O (TM: Ni, Co and Mn) bond and the second coordination shell represents NN TM-M (M: Li, Ni, Co and Mn) bond [29–30]. Obviously, all the Ni coordination shells remain almost unchanged, whereas the second coordination shell of Mn and Co shows a regular decrease in LR-/NCM11X (X = 1, 2, 3, 4, 6) samples. This indicates that more Li ions, which have less extranuclear electron, participate in Mn-M coordination and Co-M coordination. EXAFS fittings were then employed on the first two coordination shells of Mn and Co (Figs. S5 and S6) and the results are listed in Table S3 As shown in Fig. 4d, the second coordination number of Mn decreases from 6.00 to 3.78 in LR-/NCM11X (X = 1, 2, 3, 4, 6) with the increasing content of Li_2MnO_3-like domain. The second coordination number of Co shows a similar decrease trend from 6.00 to 4.79. Note that the atomic coordination in the second shell is dependent on atomic combination as we discussed above (Fig. 4b). If Co coordinates with Li in the second coordination shell, the most possible cations combination should be Li-Co-Mn. Fig. 4e shows the calculated ratio of Co content in M phase to total Co content (Co_M/Co_T), and the ratio of Co content in M phase to total transition metal cations in M phase (Co_M/TM_M). The increased Co_M/Co_T ratios indicate that the relative amount of Co in Li_2MnO_3-like domain is incremental in LR-/NCM11X (X = 1, 2, 3, 4, 6) samples. However, due to higher absolute content of Li_2MnO_3-like phase, the Co_M/TM_M ratio shows a decline trend from 26.9% to 8.1% in LR-NCM11X (X = 2, 3, 4, 6) samples. Besides, the cross-domain Co/Mn mixing would inevitably force Mn ions in Li_2MnO_3-like domain to migrate into rhombohedral domain, generating metastable Ni-Ni-Mn and Mn-Mn-Ni

Please cite this article in press as: C. Yin et al., Materials Today (2021), https://doi.org/10.1016/j.mattod.2021.10.020

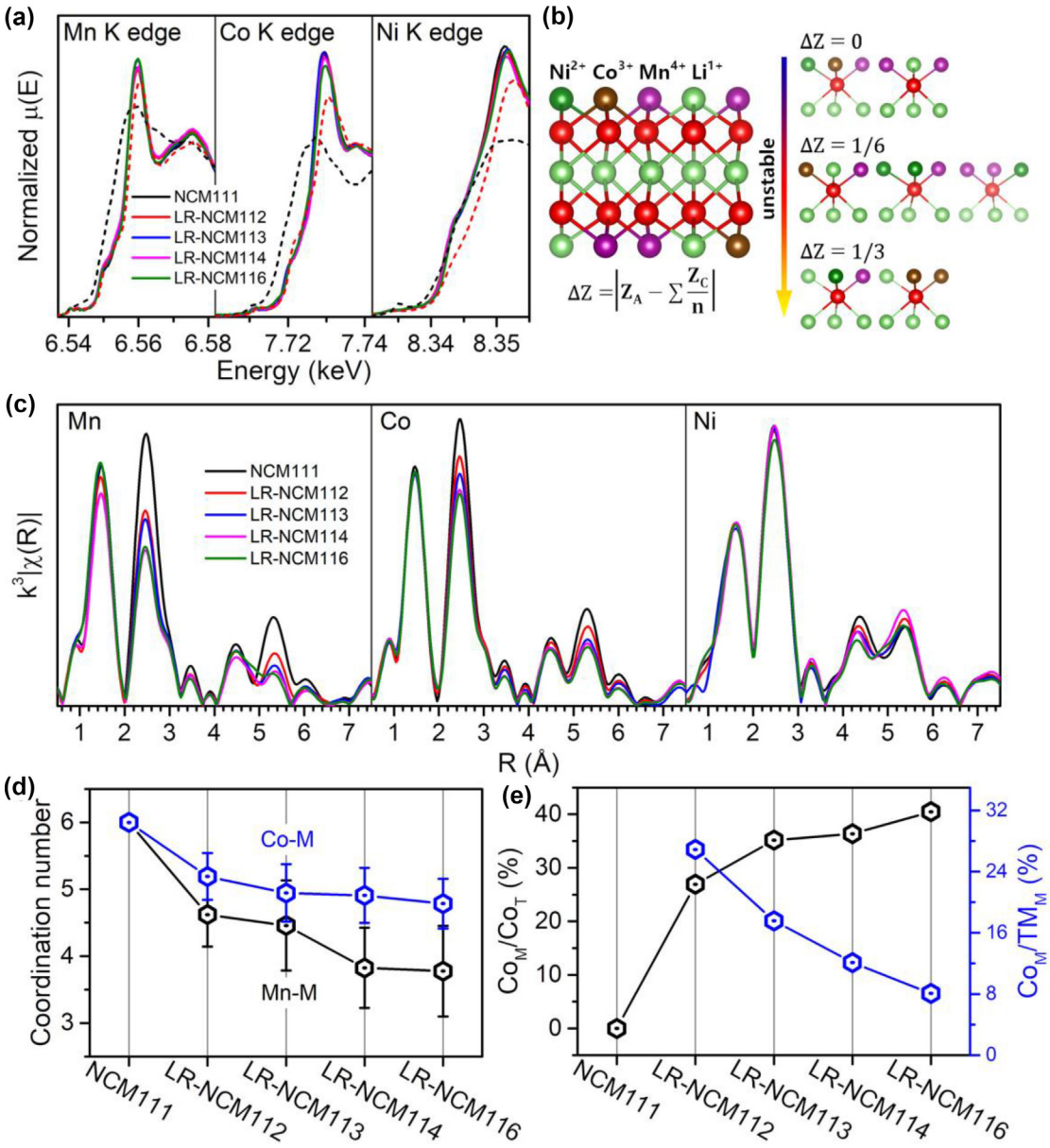

FIGURE 4

Atomic-scale structural analysis for local structure. (a) K-edge XANES of Mn, Co and Ni for LR-/NCM11X (X = 1, 2, 3, 4, 6) samples. The K-edge XANES of references (Li_2MnO_3, $LiCoO_2$ and $LiNiO_2$) are plotted by red dashed lines and the K-edge XANES of references (Mn_2O_3, CoO and $Ni(OH)_2$) are plotted by black dashed lines. (b) Schematic of atomic coordination centered on the oxygen atom. According to Pauling's electrostatic valence rule, the stability of a certain coordination configuration is determined by the valence difference between cations and the centered anion. (c) EXAFS of Mn, Co and Ni for LR-/NCM11X (X = 1, 2, 3, 4, 6) samples. (d) Fitted coordination numbers of Co and Mn in second coordination shells. (e) Calculated ratio of Co content in M phase to total Co content (black), and the ratio of Co content in M phase to total transition metal cations in M phase (blue).

combinations. These metastable combinations can be observed in $LiNi_{0.5}Mn_{0.5}O_2$ cathode material, which usually manifest a low thermal and electrochemically cycling stability [31,32].

Electrochemical activation of Li_2MnO_3-like domain

The electrochemical measurements were used to investigate the activation process of Li_2MnO_3-like domain. Fig. 5a shows the charge–discharge profiles of LR-/NCM11X (X = 1, 2, 3, 4, 6) samples under the voltage range of 2.0–4.8 V *vs.* Li^+/Li^0 at 0.1 C. All the samples show a slope region below 4.45 V and a plateau region at around 4.5 V during first charge process except for NCM111. For Li-rich layered cathodes, the capacities in the slope region (<4.45 V) are ascribed to cationic redox (Ni and Co redox) and the capacities on the plateau region come from oxygen redox [33]. As the X becomes larger in LR-NCM11X (X = 2, 3, 4, 6), the capacities on the plateau region increase from 115 mAh g^{-1} to 239 mAh g^{-1}. On the contrary, the capacities from cationic redox reduce from 178 mAh g^{-1} to 92 mAh g^{-1}, due to more inactive Mn^{4+} ions in materials. Although the charge capacities of LR-/NCM11X (X = 1, 2, 3, 4, 6) increasewith increased X values, the highest discharge capacities (~288 mAh g^{-1}) were delivered by LR-NCM114 composition.

Please cite this article in press as: C. Yin et al., Materials Today (2021), https://doi.org/10.1016/j.mattod.2021.10.020

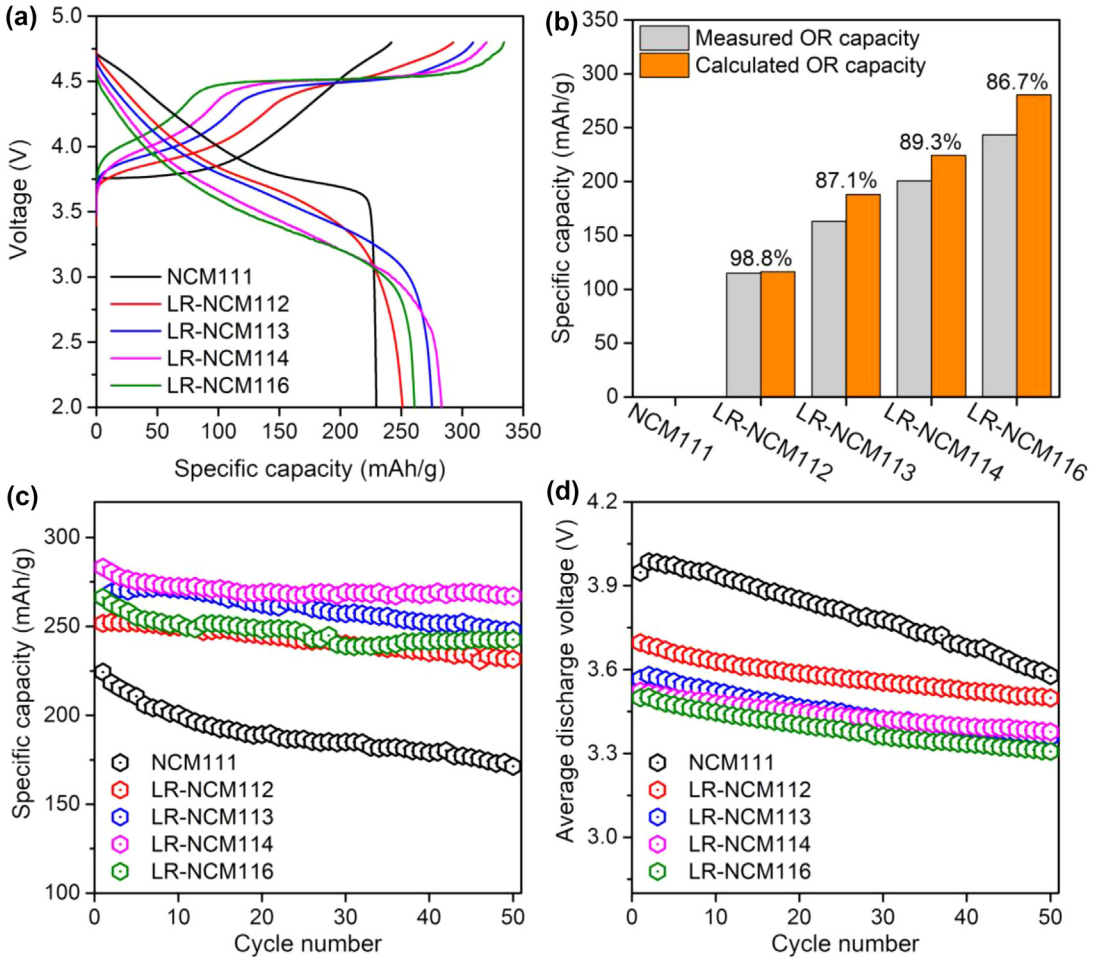

FIGURE 5

Activation of Li_2MnO_3-like domain in Li-rich layered cathode materials. (a) Charge-discharge voltage profiles of LR-/NCM11X (X = 1, 2, 3, 4, 6) samples. (b) Measured oxygen redox (OR) capacity in the plateau region (>4.45 V) versus ultimate OR capacity calculated from complete activation of Li_2MnO_3–like domain. The Li_2MnO_3–like domain fractions are obtained from Joint SXRD/TOF-ND refinements. (c) The cycling capacities of LR-/NCM11X (X = 1, 2, 3, 4, 6) samples. (d) The average discharge voltage (specific energy divided by specific capacity) decay of LR-/NCM11X (X = 1, 2, 3, 4, 6) samples.

In light of dramatic kinetics improvement by Co doping [34], it is not surprising that the relatively lower discharge capacities of low-Co/high-Mn samples (e.g. LR-NCM116) at all tested rates (Fig. S7). To further study their kinetics, GITT was applied to quantify the Li diffusion coefficient (Figs. S8 and S9). The large polarization potentials are observed in low-Co/high-Mn samples on the plateau region (Fig. S10a), indicating a sluggish structural rearrangement process triggered by oxygen redox [35]. Figs. S10b and S10c show the calculated Li diffusion coefficients during charge and discharge. The decline of Li diffusion coefficients is synchronized with the oxygen redox [17]. Furthermore, we observed that the cationic redox voltages of LR-NCM11X (X = 2, 3, 4, 6) samples in the slope region increase with increased X values (Fig. S11). This phenomenon cannot be explained by slow kinetics and resulting overpotential. Fig. S8 shows the cationic redox overpotential in the slope region does not increase with X increasing values in LR-NCM11X (from X = 2 to X = 6). The obvious voltage increase of cationic redox should be ascribed to the cross-domain Co/Mn mixing we proposed above, which leads to weakened TM-O covalency induced by the electron localization effect of Mn^{4+} substitution in rhombohedral domain [36]. The electrochemical impedance (Fig. S12) and electrical conductivity (Table S4) were also tested for the samples, showing the increasing charge transfer impedances and decreasing electrical conductivities as X becomes larger in LR-/NCM11X (X = 1, 2, 3, 4, 6) samples.

It is worth noting that even though the slow kinetics of low-Co/high-Mn samples, the activation of lattice oxygen is still achieved during the first charge process. Fig. 5b shows the measured oxygen redox capacities on the plateau region and theoretical oxygen redox capacities calculated by fully delithiating Li_2MnO_3-like domain (phase fraction of Li_2MnO_3-like domain were obtain by joint refinements). The small differences between the measured and calculated oxygen redox capacities can be observed in high-Mn samples, of which the LR-NCM116 has reached up to a Mn ratio of 75%. The oxygen redox activation of low-Co/high-Mn samples to large extent is due to the unique coordination configuration of Co. To further evaluate the activation degrees of LR-/NCM11X (X = 1, 2, 3, 4, 6) samples, galvanostatic cycling tests were performed. The stepwise activation process cannot be observed in all samples, demonstrating the high activation degrees of LR-/NCM11X (X = 1, 2, 3, 4, 6) sam-

Please cite this article in press as: C. Yin et al., Materials Today (2021), https://doi.org/10.1016/j.mattod.2021.10.020

ples during the initial cycle (Fig. 5c). The discharge voltage (specific energy divided by specific capacity) decay of LR-/NCM11X (X = 1, 2, 3, 4, 6) samples is plotted in Fig. 5d and Fig. S13. It should be noted that the voltage decay and energy density fade (Fig. S14) of NCM111 are faster than those of LR-NCM11X (X = 2, 3, 4, 6) samples. The NCM111 sample may suffer from severe surface damage and passivation under high voltage cycling because of irreversible oxidation of lattice oxygen, which leads to impedance increase during cycling [37]. In addition, we observed that the Coulombic efficiencies for all samples cannot reach 99.9% (Fig. S15), including NCM111, which calls for further study on high-voltage electrolyte [38,39].

Structure analysis for the cycled materials

The crystal structure of the samples after one cycle was also characterized by SXRD and TOF-NPD. Unlike the pristine materials, the SXRD patterns of the cycled samples show negligible super-lattice peaks (Figs. S16–S20). The disappearance of super-lattice peaks strongly indicates that the in-plane ordering of $LiMn_6$ honeycomb structure was disturbed after the oxygen redox activation. Hence, the SXRD/NPD joint *Rietveld* refinements were carried out with a single R $\bar{3}$ m phase. The refined parameters a, c and Li_{3a}/Ni_{3b} mixing degrees were summarized in Fig. S21. The changes of lattice parameters a and c indicate that the structures of the cycled samples are much different from the pristine samples, which is likely due to the structure rearrangement during cycling [35,40]. After cycling, the increase of vacancies and the magnetic frustration [41] can also induce anti-site defects as shown in the summarized Li_{3a}/Ni_{3b} mixing degrees. Interestingly, Li-rich samples can almost maintain the long-range ordering and structural integrity after 50 cycles. Take LR-NCM114 for example as shown in Fig. S22, it is hard to detect the phase transition from layered to spinel structure.

No obvious changes of Ni, Co and Mn K-edge positions are found in XANES results for the cycled samples (Fig. S23), indicating the oxidation state of cations among the samples are basically identical. The overlapping XANES of the cycled samples and pristine NCM111 suggest the oxidation states of Ni, Co and Mn in the cycled samples return to +2, +3 and +4, respectively. The RDF patterns based on EXAFS results exhibit the coordination environments of Ni, Co and Mn (Fig. 6a). The Mn-M coordination shells are still much lower than Mn-O coordination shells in low-Co/high-Mn samples (LR-NCM114 and LR-NCM116), implying that even when the $LiMn_6$ honeycomb structure is disturbed after cycling, Mn ions maintain coordination with a small amount of Li or vacancies. Further analysis was performed by fittings (Figs. S24–S26). Note that the amount of oxygen loss from the lattice is actually small (<5%) compared to the total lattice oxygen [42]. Hence, the first coordination number of TM can be approximately set as 6. The differences of the first coordination shells in LR-/NCM11X (X = 1, 2, 3, 4, 6) samples mostly originate from local structural distortion [43]. The second coordination number of Mn decreases from 6.00 to 4.93 in LR-/NCM11X (X = 1, 2, 3, 4, 6) samples, while the coordination numbers of Ni-TM and Co-TM cannot be obtained precisely because of the large analytical error caused by a distortion factor and coordination number coupling in a single shell (Tables S5–S7). On the other hand, the distortion factors σ^2 of Ni-O, Co-O and Mn-O coordination all increase after cycling (Fig. 6b–d), which is consistent with more disordered structure after activation. The increasing trend of σ^2 factors are quite different between Ni-O coordination and Co-O (Mn-O)

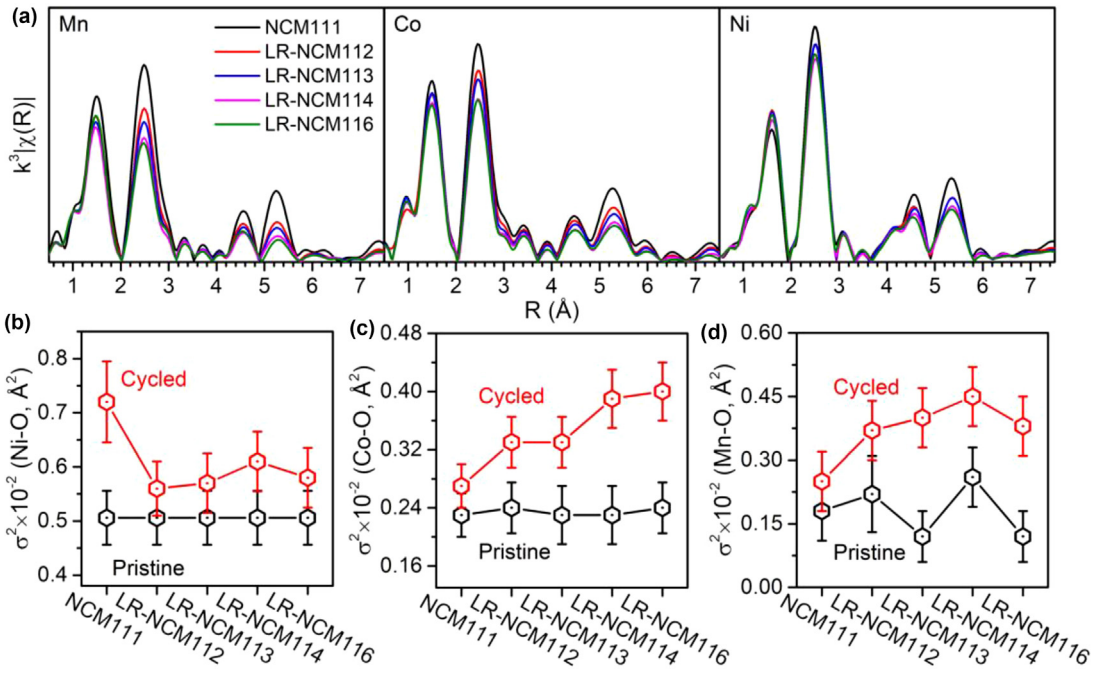

FIGURE 6

Structural analysis for cycled samples. (a) EXAFS of Mn, Co and Ni for cycled LR-/NCM11X (X = 1, 2, 3, 4, 6) samples. (b–d) Fitted distortion factors σ^2 of Ni–O, Co–O and Mn–O coordination environments for cycled samples (red). The fitted distortion factors σ^2 for pristine samples (black) are also plotted for comparison.

Please cite this article in press as: C. Yin et al., Materials Today (2021), https://doi.org/10.1016/j.mattod.2021.10.020

coordination. NCM111 sample shows a higher σ^2 value of Ni-O than those of LR-NCM11X (X = 2, 3, 4, 6) samples after cycling, while Li-rich samples exhibit a higher σ^2 value of Co–O and Mn–O than that of NCM111. Generally, the oxygen redox reaction is not completely reversible, which can disturb TM-O coordination and lead to the increase of σ^2. In case of NCM111, the oxygen coordinated with Ni is more active [44–46], and thus the σ^2 of Ni-O for cycled NCM111 increases more than that of Co–O and Mn–O. In case of Li-rich samples, due to unique Li-O-Li configuration, the oxygen in Li_2MnO_3-like domain becomes more active and accounts for significant increase of σ^2 of Mn–O. It is observed that the σ^2 of Co–O also increases drastically in Li-rich samples, which coincides with our structural analysis results that Co can intrude into Li_2MnO_3-like domain and regulate oxygen redox process.

Discussion

The excess capacities observed in Li-rich layered cathodes are believed to originate from oxygen redox of Li_2MnO_3-like domain [42]. However, the fast and complete activation of the Li_2MnO_3-like domain remains challenging, especially for high-Mn materials. We designed and synthesized a series of Li-rich layered cathodes for systematic structural characterizations to pinpoint the "sally port" for understanding the activation of Li_2MnO_3-like domain.

First, we inspect the long-range structures of LR-/NCM11X (X = 1, 2, 3, 4, 6) samples (Fig. 2). The changes of lattice parameters, phase fractions and atoms mixing degrees are determined by refinements. No obvious correlation is found between long-range structure and activation of Li_2MnO_3-like domain. These results guide us to delve into short-range structural changes of different samples. A common defect, stacking fault of transition metal layer is also identified in our work (Fig. 3). Some studies have regarded stacking faults as the key to activate Li_2MnO_3-like domain [7,15]. We synthesized the pure Li_2MnO_3 material as an example to show that the high degree of stacking faults is insufficient to achieve fast activation of Li_2MnO_3 (Figs. S27 and S28). Similar phenomenon was also reported by previous work [26], revealing that the ordering of $LiMn_6$ honeycomb structure or domain length may play an important role in the activation process. Despite the large domain length of LR-NCM116 sample, almost full activation can be achieved (Fig. 5), indicating the ordering of $LiMn_6$ honeycomb structure or domain length may have little impact on activation. Note that the high degree of activation in the first charge process was also observed in micron-size single crystalline Li-rich layered cathode [47,48]. The SEM morphology characterization also demonstrates the weak correlation between primary particle size and activation of Li_2MnO_3-like domain (Fig. S29).

We then explore the atomic-scale local structure of LR-/NCM11X (X = 1, 2, 3, 4, 6) samples by EXAFS fittings. In the second coordination shell (in-plane cationic ordering), the decrease of the coordination numbers of Mn demonstrates the increase of the $LiMn_6$ honeycomb structure, as well as Li_2MnO_3-like domain (Fig. 4c and d). The second coordination shells of Ni remain almost the same among the samples. The high peak intensity also indicates that Ni are only surrounded by transition metal elements in the second coordination shell, which is a typical structural feature in conventional NCM layered materials. In other words, Ni does not participate in the formation of Li_2MnO_3-like domain and contributes little to the activation process. This could explain why Co-free Li-rich layered cathodes are not easy to be fully activated [49]. As for Co, we note a drastic intensity reduction of the second shells due to Co-Li coordination. This implies that the Co is able to intrude into Li_2MnO_3-like domain and modulate the electronic structure of oxygen in Li_2MnO_3-like domain. The Co-3d bands across the top of the O-2p bands can potentially bridge the charge transfer path from lattice oxygen [50], which facilitates the activation of Li_2MnO_3 phase. Furthermore, the proportion of Co involved in the formation of Li_2MnO_3 phase becomes larger as the total Co content decreases, implying that low-Co samples can maximize the effect of Co on promoting activation (Fig. 4e). The structure analysis for the cycled samples further confirms the special role of Co in the activation of oxygen in Li_2MnO_3-like domain (Fig. 6). The more pronounced increases of distortion factors can be observed on Co–O and Mn–O coordination in Li-rich samples, indicating that electrochemical activation of lattice oxygen is a region-selective reaction, which mainly involves the oxygen atoms coordinated with Co and Mn. We infer that the dopant cation in Li_2MnO_3-like domain, with 3d energy bands across the top of the O-2p bands, may offer a similar role as Co to promote activation of Li-rich layered oxides.

Conclusions

In summary, a series of layered cathode materials, LR-/NCM11X (X = 1, 2, 3, 4, 6) with stepwise increase of Mn content were designed and synthesized to study the activation process of oxygen redox. The long- and short-range structural characteristics of these materials have been investigated by SXRD, TOF-NPD and EXAFS, focusing on the local structural changes of Li_2MnO_3-like domain. Stacking faults of transition metal layers and disordered $LiMn_6$ honeycomb structure in Li_2MnO_3-like domain appear in the serial samples, whereas their effects on activating Li_2MnO_3-like domain are limited. The Co mixing in Li_2MnO_3-like domain is revealed and its effect on oxygen redox activation is proposed. It is demonstrated that a small proportion of Co/Mn substitution in Li_2MnO_3-like domain is required for activation of reversible oxygen redox in Li-rich cathode materials. Our findings elucidate the unique function of Co in the activation of oxygen redox, and call for further composition tunings of Li_2MnO_3-like domain to enable high energy density for next-generation rechargeable batteries.

CRediT authorship contribution statement

Chong Yin: Conceptualization, Formal analysis, Investigation, Methodology, Validation, Visualization, Writing – original draft. **Zhining Wei:** Investigation, Validation, Resources. **Minghao Zhang:** Investigation, Methodology, Visualization, Writing – original draft. **Bao Qiu:** Conceptualization, Investigation, Writing – review & editing, Supervision, Funding acquisition, Project administration. **Yuhuan Zhou:** Investigation, Validation. **Yingguo Xiao:** Methodology, Resources. **Dong Zhou:** Methodology, Resources. **Liang Yun:** Investigation, Valida-

Please cite this article in press as: C. Yin et al., Materials Today (2021), https://doi.org/10.1016/j.mattod.2021.10.020

tion. **Cheng Li:** Methodology, Resources. **Qingwen Gu:** Validation, Resources. **Wen Wen:** Methodology, Resources. **Xiao Li:** Investigation, Validation. **Xiaohui Wen:** Investigation, Validation. **Zhepu Shi:** Investigation, Validation. **Lunhua He:** Methodology, Resources. **Ying Shirley Meng:** Conceptualization, Writing – review & editing, Supervision. **Zhaoping Liu:** Conceptualization, Writing – review & editing, Supervision, Funding acquisition, Project administration.

Declaration of Competing Interest

The authors declare that they have no known competing financial interests or personal relationships that could have appeared to influence the work reported in this paper.

Acknowledgements

This work was supported by the National Key Research and Development Program of China (Grant No. 2016YFB0100100), and the National Natural Science Foundation of China (Grant No. 21703271 and 21773279), Natural Science Foundation of Ningbo (Grant No. 202003N4030), and S&T Innovation 2025 Major Special Program of Ningbo (Grant No. 2018B10081). YSM and MZ thank the Zable endowed chair fund for supporting the international collaboration. The authors thank the beam time from beamline BL14B (SSRF), the beam time at GPPD granted from China Spallation Neutron Source (CSNS) and beamline KMC-2 (BESSY), beamline BL11B (SSRF) for providing the beam time and helps during experiments. A portion of this research used resources at the Spallation Neutron Source, a DOE Office of Science User Facility operated by the Oak Ridge National Laboratory.

Declaration of Competing Interests

The authors declare no competing financial interests.

Appendix A. Supplementary data

Supplementary data to this article can be found online at https://doi.org/10.1016/j.mattod.2021.10.020.

References

[1] J.M. Tarascon, M. Armand, Issues and challenges facing rechargeable lithium batteries, Nature 414 (2001) 359–367, https://doi.org/10.1038/35104644.

[2] B. Dunn, H. Kamath, J.M. Tarascon, Electrical energy storage for the grid: a battery of choices, Science 334 (2011) 928–935, https://doi.org/10.1126/science.1212741.

[3] M. Weiss, F.J. Simon, M.R. Busche, T. Nakamura, D. Schröder, F.H. Richter, J. Janek, From Liquid- to Solid-State Batteries: Ion Transfer Kinetics of Heteroionic Interfaces, Electrochem. Energy Rev. 3 (2020) 221–238, https://doi.org/10.1007/s41918-020-00062-7.

[4] M. Li, T. Liu, X. Bi, Z. Chen, K. Amine, C. Zhong, J. Lu, Cationic and anionic redox in lithium-ion based batteries, Chem. Soc. Rev. 49 (2020) 1688–1705, https://doi.org/10.1039/c8cs00426a.

[5] D.-H. Seo, J. Lee, A. Urban, R. Malik, S. Kang, G. Ceder, The structural and chemical origin of the oxygen redox activity in layered and cation-disordered Li-excess cathode materials, Nat. Chem. 8 (2016) 692–697, https://doi.org/10.1038/nchem.2524.

[6] P. Kalyani, S. Chitra, T. Mohan, S. Gopukumar, Lithium metal rechargeable cells using Li_2MnO_3 as the positive electrode, J. Power Sources 80 (1999) 103–106, https://doi.org/10.1016/S0378-7753(99)00066-X.

[7] D.Y.W. Yu, K. Yanagida, Y. Kato, H. Nakamura, Electrochemical activities in Li_2MnO_3, J. Electrochem. Soc. 156 (2009) A417–A424, https://doi.org/10.1149/1.3110803.

[8] M.M. Thackeray, S.-H. Kang, C.S. Johnson, J.T. Vaughey, R. Benedek, S.A. Hackney, Li_2MnO_3-stabilized $LiMO_2$ (M = Mn, Ni, Co) electrodes for lithium-ion batteries, J. Mater. Chem. 17 (2007) 3112–3125, https://doi.org/10.1039/b702425h.

[9] B. Qiu, M. Zhang, Y. Xia, Z. Liu, Y.S. Meng, Understanding and controlling anionic electrochemical activity in high-capacity oxides for next generation Li-ion batteries, Chem. Mater. 29 (2017) 908–915, https://doi.org/10.1021/acs.chemmater.6b04815.

[10] S.H. Kang K. Amine Synthesis and electrochemical properties of layer-structured 0.5Li(Ni0.5Mn0.5)O2–0.5Li(Li1/3Mn2/3)O2 solid mixture J. Power Sources 124 (2003) 533 537 10.1016/s0378-7753(03)00804-8

[11] L. Zhang K. Takada N. Ohta K. Fukuda T. Sasaki Synthesis of (1–2x)LiNi1/2Mn1/2O2·xLi[Li1/3Mn2/3]O2·xLiCoO2 ($0 \le x \le 0.5$) electrode materials and comparative study on cooling rate J. Power Sources 146 (2005) 598 601 10.1016/j.jpowsour.2005.03.122

[12] R.-P. Qing, J.-L. Shi, D.-D. Xiao, X.-D. Zhang, Y.-X. Yin, Y.-B. Zhai, L. Gu, Y.-G. Guo, Enhancing the kinetics of Li-rich cathode materials through the pinning effects of gradient surface Na^+ doping, Adv. Energy Mater. 6 (2016) 1501914, https://doi.org/10.1002/aenm.201501914.

[13] F. Wu, G.T. Kim, M. Kuenzel, H. Zhang, J. Asenbauer, D. Geiger, U. Kaiser, S. Passerini, Elucidating the effect of iron doping on the electrochemical performance of cobalt-free lithium-rich layered cathode materials, Adv. Energy Mater. 9 (2019) 1902445, https://doi.org/10.1002/aenm.201902445.

[14] C.-C. Wang, A. Manthiram, Influence of cationic substitutions on the first charge and reversible capacities of lithium-rich layered oxide cathodes, J. Mater. Chem. A 1 (2013) 10209–10217, https://doi.org/10.1039/c3ta11703k.

[15] J. Liu, M. Hou, J. Yi, S. Guo, C. Wang, Y. Xia, Improving the electrochemical performance of layered lithium-rich transition-metal oxides by controlling the structural defects, Energ, Environ. Sci. 7 (2014) 705–714, https://doi.org/10.1039/c3ee41664j.

[16] Y. Sun, H. Cong, L. Zan, Y. Zhang, Oxygen vacancies and stacking faults introduced by low-temperature reduction improve the electrochemical properties of Li_2MnO_3 nanobelts as lithium-ion battery cathodes, ACS Appl. Mater. Inter. 9 (2017) 38545–38555, https://doi.org/10.1021/acsami.7b12080.

[17] C. Yin, L. Wan, B. Qiu, F. Wang, W. Jiang, H. Cui, J. Bai, S. Ehrlich, Z. Wei, Z. Liu, Boosting energy efficiency of Li-rich layered oxide cathodes by tuning oxygen redox kinetics and reversibility, Energy Storage Mater. 35 (2021) 388–399, https://doi.org/10.1016/j.ensm.2020.11.034.

[18] B.H. Toby, R.B. Von Dreele, GSAS-II: the genesis of a modern open-source all purpose crystallography software package, J. Appl. Crystallogr. 46 (2013) 544–549, https://doi.org/10.1107/s0021889813003531.

[19] M. Casas-Cabanas, M. Reynaud, J. Rikarte, P. Horbach, J. Rodríguez-Carvajal, FAULTS: a program for refinement of structures with extended defects, J. Appl. Crystallogr. 49 (2016) 2259–2269, https://doi.org/10.1107/s1600576716014473.

[20] B. Ravel, M. Newville, ATHENA, ARTEMIS, HEPHAESTUS: data analysis for X-ray absorption spectroscopy using IFEFFIT, J. Synchrotron Radiat. 12 (2005) 537–541, https://doi.org/10.1107/S0909049505012719.

[21] T. Sarkar, K.R. Prakasha, M.D. Bharadwaj, A.S. Prakash, Lithium diffusion study in Li_2MnO_3 and $Li_{1.17}Ni_{0.17}Mn_{0.67}O_2$: a combined experimental and computational approach, Phys. Chem. Chem. Phys. 19 (2017) 31724–31730, https://doi.org/10.1039/c7cp06458f.

[22] Z. Lu, D.D. MacNeil, J.R. Dahn, Layered cathode materials $Li[Ni_xLi_{(1/3-2x/3)}Mn_{(2/3-x/3)}]O_2$ for lithium-ion batteries, Electrochem. Solid St. 4 (2001) A191–A194, https://doi.org/10.1149/1.1407994.

[23] H.M. Rietveld, The crystal structure of some alkaline earth metal uranates of the typeM3UO6, Acta Crystallographica 20 (1966) 508–513, https://doi.org/10.1107/s0365110x66001154.

[24] R. Shunmugasundaram, R.S. Arumugam, J.R. Dahn, A study of stacking faults and superlattice ordering in some Li-rich layered transition metal oxide positive electrode materials, J. Electrochem. Soc. 163 (2016) A1394–A1400, https://doi.org/10.1149/2.1221607jes.

[25] M.M. Thackeray, S.H. Kang, C.S. Johnson, J.T. Vaughey, S.A. Hackney, Comments on the structural complexity of lithium-rich $Li_{1+x}M_{1-x}O_2$ electrodes (M = Mn, Ni, Co) for lithium batteries, Electrochem. Commun. 8 (2006) 1531–1538, https://doi.org/10.1016/j.elecom.2006.06.030.

[26] J. Serrano-Sevillano, M. Reynaud, A. Saracibar, T. Altantzis, S. Bals, G. Van Tendeloo, M. Casas-Cabanas, Enhanced electrochemical performance of Li-rich cathode materials through microstructural control, Phys. Chem. Chem. Phys. 20 (2018) 23112–23122, https://doi.org/10.1039/c8cp04181d.

[27] B.J. Hwang, Y.W. Tsai, D. Carlier, G. Ceder, A combined computational/experimental study on $LiNi_{1/3}Co_{1/3}Mn_{1/3}O_2$, Chem. Mater. 15 (2003) 3676–3682, https://doi.org/10.1021/cm030299v.

[28] L. Pauling, The principles determining the structure of complex ionic crystals, J. Am. Chem. Soc. 51 (1929) 1010–1026, https://doi.org/10.1021/ja01379a006.

[29] J. Rana, M. Stan, R. Kloepsch, J. Li, G. Schumacher, E. Welter, I. Zizak, J. Banhart, M. Winter, Structural changes in Li_2MnO_3 cathode material for Li-ion batteries, Adv. Energy Mater. 4 (2014) 1300998, https://doi.org/10.1002/aenm.201300998.

[30] Y.W. Tsai, B.J. Hwang, G. Ceder, H.S. Sheu, D.G. Liu, J.F. Lee, In-situ X-ray absorption spectroscopic study on variation of electronic transitions and local structure of $LiNi_{1/3}Co_{1/3}Mn_{1/3}O_2$ cathode material during electrochemical cycling, Chem. Mater. 17 (2005) 3191–3199, https://doi.org/10.1021/cm048027v.

[31] J. Breger N. Dupre P.J. Chupas P.L. Lee T. Proffen J.B. Parise C.P. Grey Short- and long-range order in the positive electrode material, Li(NiMn)0.5O2: a joint X-ray and neutron diffraction, pair distribution function analysis and NMR study J Am Chem Soc 127 (2005) 7529 7537 10.1021/ja050697u

[32] W.S. Yoon Y. Paik X.Q. Yang M. Balasubramanian J. McBreen C.P. Grey Investigation of the local structure of the LiNi0.5Mn0.5O2 cathode material during electrochemical cycling by X-ray absorption and NMR spectroscopy Electrochem. Solid St. 5 (2002) A263 A266 10.1149/1.1513001

[33] G. Assat, J.M. Tarascon, Fundamental understanding and practical challenges of anionic redox activity in Li-ion batteries, Nat. Energy 3 (2018) 373–386, https://doi.org/10.1038/s41560-018-0097-0.

[34] J. Kou, L. Chen, Y. Su, L. Bao, J. Wang, N. Li, W. Li, M. Wang, S. Chen, F. Wu, The role of cobalt content in improving low temperature performance of layered lithium-rich cathode materials for Li-ion batteries, ACS Appl. Mater. Inter. 7 (2015) 17910–17918, https://doi.org/10.1021/acsami.5b04514.

[35] G. Assat, S.L. Glazier, C. Delacourt, J.-M. Tarascon, Probing the thermal effects of voltage hysteresis in anionic redox-based lithium-rich cathodes using isothermal calorimetry, Nat. Energy 4 (2019) 647–656, https://doi.org/10.1038/s41560-019-0410-6.

[36] X. Wang, X. Fan, X. Yu, S. Bak, Z. Shadike, I. Waluyo, A. Hunt, S.D. Senanayake, H. Li, L. Chen, C. Wang, R. Xiao, E. Hu, X.Q. Yang, The Role of Electron Localization in Covalency and Electrochemical Properties of Lithium-Ion Battery Cathode Materials, Adv. Funct. Mater. 31 (2020) 2001633, https://doi.org/10.1002/adfm.202001633.

[37] S.H. Song, M. Cho, I. Park, J.G. Yoo, K.T. Ko, J. Hong, J. Kim, S.K. Jung, M. Avdeev, S. Ji, S. Lee, J. Bang, H. Kim, High-voltage-driven surface structuring and electrochemical stabilization of Ni-rich layered cathode materials for Li rechargeable batteries, Adv. Energy Mater. 10 (2020) 2000521, https://doi.org/10.1002/aenm.202000521.

[38] X. Zhang, L. Zou, Z. Cui, H. Jia, M.H. Engelhard, B.E. Matthews, X. Cao, Q. Xie, C. Wang, A. Manthiram, J.-G. Zhang, W. Xu, Stabilizing ultrahigh-nickel layered oxide cathodes for high-voltage lithium metal batteries, Materials Today 44 (2021) 15–24, https://doi.org/10.1016/j.mattod.2021.01.013.

[39] C. Cui, X. Fan, X. Zhou, J. Chen, Q. Wang, L. Ma, C. Yang, E. Hu, X.Q. Yang, C. Wang, Structure and Interface Design Enable Stable Li-Rich Cathode, J. Am. Chem. Soc. 142 (2020) 8918–8927, https://doi.org/10.1021/jacs.0c02302.

[40] A. Singer, M. Zhang, S. Hy, D. Cela, C. Fang, T.A. Wynn, B. Qiu, Y. Xia, Z. Liu, A. Ulvestad, N. Hua, J. Wingert, H. Liu, M. Sprung, A.V. Zozulya, E. Maxey, R. Harder, Y.S. Meng, O.G. Shpyrko, Nucleation of dislocations and their dynamics in layered oxide cathode materials during battery charging, Nat. Energy 3 (2018) 641–647, https://doi.org/10.1038/s41560-018-0184-2.

[41] M. Li, J. Lu, Cobalt in lithium-ion batteries, Science 367 (2020) 979, https://doi.org/10.1126/science.aba9168.

[42] K. Luo, M.R. Roberts, R. Hao, N. Guerrini, D.M. Pickup, Y.-S. Liu, K. Edström, J. Guo, A.V. Chadwick, L.C. Duda, P.G. Bruce, Charge-compensation in 3d-transition-metal-oxide intercalation cathodes through the generation of localized electron holes on oxygen, Nat. Chem. 8 (2016) 684–691, https://doi.org/10.1038/nchem.2471.

[43] M.J. Zuba, A. Grenier, Z. Lebens-Higgins, G.J.P. Fajardo, Y. Li, Y. Ha, H. Zhou, M. S. Whittingham, W. Yang, Y.S. Meng, K.W. Chapman, L.F.J. Piper, Whither Mn Oxidation in Mn-Rich Alkali-Excess Cathodes?, ACS Energy Lett 6 (2021) 1055–1064, https://doi.org/10.1021/acsenergylett.0c02418.

[44] N. Li, S. Sallis, J.K. Papp, J. Wei, B.D. McCloskey, W. Yang, W. Tong, Unraveling the Cationic and Anionic Redox Reactions in Conventional Layered Oxide Cathode, ACS Energy Lett. 4 (2019) 2836–2842, https://doi.org/10.1021/acsenergylett.9b02147.

[45] J.H. Song, G. Yoon, B. Kim, D. Eum, H. Park, D.H. Kim, K. Kang, Anionic redox activity regulated by transition metal in lithium-rich layered oxides, Adv. Energy Mater. 10 (2020) 2001207, https://doi.org/10.1002/aenm.202001207.

[46] G.H. Lee, J. Wu, D. Kim, K. Cho, M. Cho, W. Yang, Y.M. Kang, Reversible Anionic Redox Activities in Conventional $LiNi_{1/3}$ $Co_{1/3}$ $Mn_{1/3}$ O_2 Cathodes, Angew. Chem. Int. Edit. 59 (2020) 8681–8688, https://doi.org/10.1002/anie.202001349.

[47] H. Peng, S.X. Zhao, C. Huang, L.Q. Yu, Z.Q. Fang, G.D. Wei, In Situ Construction of Spinel Coating on the Surface of a Lithium-Rich Manganese-Based Single Crystal for Inhibiting Voltage Fade, ACS Appl Mater Interfaces 12 (2020) 11579–11588, https://doi.org/10.1021/acsami.9b21271.

[48] Y. Xie, J. Yin, X. Chen, X. Liang, Y. Jin, L. Xiang, Synergistic effect of Mn^{3+} formation-migration and oxygen loss on the near surface and bulk structural changes in single crystalline lithium-rich oxides, ACS Appl. Mater. Inter. 13 (2021) 3891–3898, https://doi.org/10.1021/acsami.0c18758.

[49] D. Ye, B. Wang, Y. Chen, G. Han, Z. Zhang, D. Hulicova-Jurcakova, J. Zou, L. Wang, Understanding the stepwise capacity increase of high energy low-Co Li-rich cathode materials for lithium ion batteries, J. Mater. Chem. A 2 (2014) 18767–18774, https://doi.org/10.1039/c4ta03692a.

[50] J.B. Goodenough, Evolution of strategies for modern rechargeable batteries, Accounts Chem. Res. 46 (2013) 1053–1061, https://doi.org/10.1021/ar2002705.

Please cite this article in press as: C. Yin et al., Materials Today (2021), https://doi.org/10.1016/j.mattod.2021.10.020